

Production of K_S^0 , $K^{*\pm}(892)$ and $\phi^0(1020)$ in minimum bias events and K_S^0 and Λ^0 in jets in $p\bar{p}$ collisions at $\sqrt{s} = 1.96$ TeV

T. Aaltonen,²¹ M. Albrow,¹⁵ B. Álvarez González,⁹ S. Amerio,⁴⁰ D. Amidei,³² A. Anastassov,^{x,15} A. Annovi,¹⁷ J. Antos,¹² G. Apollinari,¹⁵ J.A. Appel,¹⁵ T. Arisawa,⁵⁴ A. Artikov,¹³ J. Asaadi,⁴⁹ W. Ashmanskas,¹⁵ B. Auerbach,⁵⁷ A. Aurisano,⁴⁹ F. Azfar,³⁹ W. Badgett,¹⁵ T. Bae,²⁵ A. Barbaro-Galtieri,²⁶ V.E. Barnes,⁴⁴ B.A. Barnett,²³ P. Barria,^{hh,42} P. Bartos,¹² M. Baucé,^{ff,40} F. Bedeschi,⁴² S. Behari,²³ G. Bellettini,^{gg,42} J. Bellinger,⁵⁶ D. Benjamin,¹⁴ A. Beretvas,¹⁵ A. Bhatti,⁴⁶ D. Bisello,^{ff,40} I. Bizjak,²⁸ K.R. Bland,⁵ B. Blumenfeld,²³ A. Bocci,¹⁴ A. Bodek,⁴⁵ D. Bortoletto,⁴⁴ J. Boudreau,⁴³ A. Boveia,¹¹ L. Brigliadori,^{ee,6} C. Bromberg,³³ E. Brucken,²¹ J. Budagov,¹³ H.S. Budd,⁴⁵ K. Burkett,¹⁵ G. Busetto,^{ff,40} P. Bussey,¹⁹ A. Buzatu,³¹ A. Calamba,¹⁰ C. Calancha,²⁹ S. Camarda,⁴ M. Campanelli,²⁸ M. Campbell,³² F. Canelli,^{11,15} B. Carls,²² D. Carlsmith,⁵⁶ R. Carosi,⁴² S. Carrillo,^{m,16} S. Carron,¹⁵ B. Casal,^{k,9} M. Casarsa,⁵⁰ A. Castro,^{ee,6} P. Catastini,²⁰ D. Cauz,⁵⁰ V. Cavaliere,²² M. Cavalli-Sforza,⁴ A. Cerri,^{f,26} L. Cerrito,^{s,28} Y.C. Chen,¹ M. Chertok,⁷ G. Chiarelli,⁴² G. Chlachidze,¹⁵ F. Chlebana,¹⁵ K. Cho,²⁵ D. Chokheli,¹³ W.H. Chung,⁵⁶ Y.S. Chung,⁴⁵ M.A. Ciocci,^{hh,42} A. Clark,¹⁸ C. Clarke,⁵⁵ G. Compostella,^{ff,40} M.E. Convery,¹⁵ J. Conway,⁷ M. Corbo,¹⁵ M. Cordelli,¹⁷ C.A. Cox,⁷ D.J. Cox,⁷ F. Crescioli,^{gg,42} J. Cuevas,^{z,9} R. Culbertson,¹⁵ D. Dagenhart,¹⁵ N. d'Ascenzo,^{w,15} M. Datta,¹⁵ P. de Barbaro,⁴⁵ M. Dell'Orso,^{gg,42} L. Demortier,⁴⁶ M. Deninno,⁶ F. Devoto,²¹ M. d'Errico,^{ff,40} A. Di Canto,^{gg,42} B. Di Ruzza,¹⁵ J.R. Dittmann,⁵ M. D'Onofrio,²⁷ S. Donati,^{gg,42} P. Dong,¹⁵ M. Dorigo,⁵⁰ T. Dorigo,⁴⁰ K. Ebina,⁵⁴ A. Elagin,⁴⁹ A. Eppig,³² R. Erbacher,⁷ S. Errede,²² N. Ershaidat,^{dd,15} R. Eusebi,⁴⁹ S. Farrington,³⁹ M. Feindt,²⁴ J.P. Fernandez,²⁹ R. Field,¹⁶ G. Flanagan,^{u,15} R. Forrest,⁷ M.J. Frank,⁵ M. Franklin,²⁰ J.C. Freeman,¹⁵ Y. Funakoshi,⁵⁴ I. Furic,¹⁶ M. Gallinaro,⁴⁶ J.E. Garcia,¹⁸ A.F. Garfinkel,⁴⁴ P. Garosi,^{hh,42} H. Gerberich,²² E. Gerchtein,¹⁵ S. Giagu,⁴⁷ V. Giakoumopoulou,³ P. Giannetti,⁴² K. Gibson,⁴³ C.M. Ginsburg,¹⁵ N. Giokaris,³ P. Giromini,¹⁷ G. Giurgiu,²³ V. Glagolev,¹³ D. Glenzinski,¹⁵ M. Gold,³⁵ D. Goldin,⁴⁹ N. Goldschmidt,¹⁶ A. Golossanov,¹⁵ G. Gomez,⁹ G. Gomez-Ceballos,³⁰ M. Goncharov,³⁰ O. González,²⁹ I. Gorelov,³⁵ A.T. Goshaw,¹⁴ K. Goulianos,⁴⁶ S. Grinstein,⁴ C. Grosso-Pilcher,¹¹ R.C. Group,^{53,15} J. Guimaraes da Costa,²⁰ S.R. Hahn,¹⁵ E. Halkiadakis,⁴⁸ A. Hamaguchi,³⁸ J.Y. Han,⁴⁵ F. Happacher,¹⁷ K. Hara,⁵¹ D. Hare,⁴⁸ M. Hare,⁵² R.F. Harr,⁵⁵ K. Hatakeyama,⁵ C. Hays,³⁹ M. Heck,²⁴ J. Heinrich,⁴¹ M. Herndon,⁵⁶ S. Hewamanage,⁵ A. Hocker,¹⁵ W. Hopkins,^{g,15} D. Horn,²⁴ S. Hou,¹ R.E. Hughes,³⁶ M. Hurwitz,¹¹ U. Husemann,⁵⁷ N. Hussain,³¹ M. Hussein,³³ J. Huston,³³ G. Introzzi,⁴² M. Iori,^{jj,47} A. Ivanov,^{p,7} E. James,¹⁵ D. Jang,¹⁰ B. Jayatilaka,¹⁴ E.J. Jeon,²⁵ S. Jindariani,¹⁵ M. Jones,⁴⁴ K.K. Joo,²⁵ S.Y. Jun,¹⁰ T.R. Junk,¹⁵ T. Kamon,^{25,49} P.E. Karchin,⁵⁵ A. Kashi,⁵ Y. Kato,^{o,38} W. Ketchum,¹¹ J. Keung,⁴¹ V. Khotilovich,⁴⁹ B. Kilminster,¹⁵ D.H. Kim,²⁵ H.S. Kim,²⁵ J.E. Kim,²⁵ M.J. Kim,¹⁷ S.B. Kim,²⁵ S.H. Kim,⁵¹ Y.K. Kim,¹¹ Y.J. Kim,²⁵ N. Kimura,⁵⁴ M. Kirby,¹⁵ S. Klimenko,¹⁶ K. Knoepfel,¹⁵ K. Kondo,^{*,54} D.J. Kong,²⁵ J. Konigsberg,¹⁶ A.V. Kotwal,¹⁴ M. Kreps,²⁴ J. Kroll,⁴¹ D. Krop,¹¹ M. Kruse,¹⁴ V. Krutelyov,^{c,49} T. Kuhr,²⁴ M. Kurata,⁵¹ S. Kwang,¹¹ A.T. Laasanen,⁴⁴ S. Lami,⁴² S. Lammel,¹⁵ M. Lancaster,²⁸ R.L. Lander,⁷ K. Lannon,^{y,36} A. Lath,⁴⁸ G. Latino,^{hh,42} T. LeCompte,² E. Lee,⁴⁹ H.S. Lee,^{g,11} J.S. Lee,²⁵ S.W. Lee,^{bb,49} S. Leo,^{gg,42} S. Leone,⁴² J.D. Lewis,¹⁵ A. Limosani,^{t,14} C.-J. Lin,²⁶ M. Lindgren,¹⁵ E. Lipeles,⁴¹ A. Lister,¹⁸ D.O. Litvintsev,¹⁵ C. Liu,⁴³ H. Liu,⁵³ Q. Liu,⁴⁴ T. Liu,¹⁵ S. Lockwitz,⁵⁷ A. Loginov,⁵⁷ D. Lucchesi,^{ff,40} J. Lueck,²⁴ P. Lujan,²⁶ P. Lukens,¹⁵ G. Lungu,⁴⁶ J. Lys,²⁶ R. Lysak,^{e,12} R. Madrak,¹⁵ K. Maeshima,¹⁵ P. Maestro,^{hh,42} S. Malik,⁴⁶ G. Manca,^{a,27} A. Manousakis-Katsikakis,³ F. Margaroli,⁴⁷ C. Marino,²⁴ M. Martínez,⁴ P. Mastrandrea,⁴⁷ K. Matera,²² M.E. Mattson,⁵⁵ A. Mazzacane,¹⁵ P. Mazzanti,⁶ K.S. McFarland,⁴⁵ P. McIntyre,⁴⁹ R. McNulty,^{j,27} A. Mehta,²⁷ P. Mehtala,²¹ C. Mesropian,⁴⁶ T. Miao,¹⁵ D. Mietlicki,³² A. Mitra,¹ H. Miyake,⁵¹ S. Moed,¹⁵ N. Moggi,⁶ M.N. Mondragon,^{m,15} C.S. Moon,²⁵ R. Moore,¹⁵ M.J. Morello,^{ii,42} J. Morlock,²⁴ P. Movilla Fernandez,¹⁵ A. Mukherjee,¹⁵ Th. Muller,²⁴ P. Murat,¹⁵ M. Mussini,^{ee,6} J. Nachtman,^{n,15} Y. Nagai,⁵¹ J. Naganoma,⁵⁴ I. Nakano,³⁷ A. Napier,⁵² J. Nett,⁴⁹ C. Neu,⁵³ M.S. Neubauer,²² J. Nielsen,^{d,26} L. Nodulman,² S.Y. Noh,²⁵ O. Norriella,²² L. Oakes,³⁹ S.H. Oh,¹⁴ Y.D. Oh,²⁵ I. Oksuzian,⁵³ T. Okusawa,³⁸ R. Orava,²¹ L. Ortolan,⁴ S. Pagan Griso,^{ff,40} C. Pagliarone,⁵⁰ E. Palencia,^{f,9} V. Papadimitriou,¹⁵ A.A. Paramonov,² J. Patrick,¹⁵ G. Pauletta,^{kk,50} M. Paulini,¹⁰ C. Paus,³⁰ D.E. Pellett,⁷ A. Penzo,⁵⁰ T.J. Phillips,¹⁴ G. Piacentino,⁴² E. Pianori,⁴¹ J. Pilot,³⁶ K. Pitts,²² C. Plager,⁸ L. Pondrom,⁵⁶ S. Poprocki,^{g,15} K. Potamianos,⁴⁴ F. Prokoshin,^{cc,13} A. Pranko,²⁶ F. Ptohos,^{h,17} G. Punzi,^{gg,42} A. Rahaman,⁴³ V. Ramakrishnan,⁵⁶ N. Ranjan,⁴⁴ I. Redondo,²⁹ P. Renton,³⁹ M. Rescigno,⁴⁷ T. Riddick,²⁸ F. Rimondi,^{ee,6} L. Ristori,^{42,15} A. Robson,¹⁹ T. Rodrigo,⁹ T. Rodriguez,⁴¹ E. Rogers,²² S. Rolli,^{i,52} R. Roser,¹⁵ F. Ruffini,^{hh,42}

* Deceased

A. Ruiz,⁹ J. Russ,¹⁰ V. Rusu,¹⁵ A. Safonov,⁴⁹ W.K. Sakumoto,⁴⁵ Y. Sakurai,⁵⁴ L. Santi^{kk},⁵⁰ K. Sato,⁵¹ V. Saveliev^w,¹⁵ A. Savoy-Navarro^{aa},¹⁵ P. Schlabach,¹⁵ A. Schmidt,²⁴ E.E. Schmidt,¹⁵ T. Schwarz,¹⁵ L. Scodellaro,⁹ A. Scribano^{hh},⁴² F. Scuri,⁴² S. Seidel,³⁵ Y. Seiya,³⁸ A. Semenov,¹³ F. Sforza^{hh},⁴² S.Z. Shalhout,⁷ T. Shears,²⁷ P.F. Shepard,⁴³ M. Shimojima^v,⁵¹ M. Shochet,¹¹ I. Shreyber-Tecker,³⁴ A. Simonenko,¹³ P. Sinervo,³¹ K. Sliwa,⁵² J.R. Smith,⁷ F.D. Snider,¹⁵ A. Soha,¹⁵ V. Sorin,⁴ H. Song,⁴³ P. Squillacioti^{hh},⁴² M. Stancari,¹⁵ R. St. Denis,¹⁹ B. Stelzer,³¹ O. Stelzer-Chilton,³¹ D. Stentz^x,¹⁵ J. Strologas,³⁵ G.L. Strycker,³² Y. Sudo,⁵¹ A. Sukhanov,¹⁵ I. Suslov,¹³ K. Takemasa,⁵¹ Y. Takeuchi,⁵¹ J. Tang,¹¹ M. Tecchio,³² P.K. Teng,¹ J. Thom^g,¹⁵ J. Thome,¹⁰ G.A. Thompson,²² E. Thomson,⁴¹ D. Toback,⁴⁹ S. Tokar,¹² K. Tollefson,³³ T. Tomura,⁵¹ S. Torre,¹⁷ D. Torretta,¹⁵ P. Totaro,⁴⁰ M. Trovatoⁱⁱ,⁴² F. Ukegawa,⁵¹ S. Uozumi,²⁵ A. Varganov,³² F. Vázquez^m,¹⁶ G. Velev,¹⁵ C. Vellidis,¹⁵ M. Vidal,⁴⁴ I. Vila,⁹ R. Vilar,⁹ J. Vizán,⁹ M. Vogel,³⁵ G. Volpi,¹⁷ P. Wagner,⁴¹ R.L. Wagner,¹⁵ T. Wakisaka,³⁸ R. Wallny,⁸ C. Wang,¹⁴ S.M. Wang,¹ A. Warburton,³¹ D. Waters,²⁸ W.C. Wester III,¹⁵ D. Whiteson^b,⁴¹ A.B. Wicklund,² E. Wicklund,¹⁵ S. Wilbur,¹¹ F. Wick,²⁴ H.H. Williams,⁴¹ J.S. Wilson,³⁶ P. Wilson,¹⁵ B.L. Winer,³⁶ P. Wittich^g,¹⁵ S. Wolbers,¹⁵ H. Wolfe,³⁶ T. Wright,³² X. Wu,¹⁸ Z. Wu,⁵ K. Yamamoto,³⁸ D. Yamato,³⁸ T. Yang,¹⁵ U.K. Yang^r,¹¹ Y.C. Yang,²⁵ W.-M. Yao,²⁶ G.P. Yeh,¹⁵ K. Yiⁿ,¹⁵ J. Yoh,¹⁵ K. Yorita,⁵⁴ T. Yoshida^l,³⁸ G.B. Yu,¹⁴ I. Yu,²⁵ S.S. Yu,¹⁵ J.C. Yun,¹⁵ A. Zanetti,⁵⁰ Y. Zeng,¹⁴ C. Zhou,¹⁴ and S. Zucchelli^{ee6}

(CDF Collaboration[†])

¹*Institute of Physics, Academia Sinica, Taipei, Taiwan 11529, Republic of China*

²*Argonne National Laboratory, Argonne, Illinois 60439, USA*

³*University of Athens, 157 71 Athens, Greece*

⁴*Institut de Física d'Altes Energies, ICREA, Universitat Autònoma de Barcelona, E-08193, Bellaterra (Barcelona), Spain*

⁵*Baylor University, Waco, Texas 76798, USA*

⁶*Istituto Nazionale di Fisica Nucleare Bologna, ^{ee}University of Bologna, I-40127 Bologna, Italy*

⁷*University of California, Davis, Davis, California 95616, USA*

⁸*University of California, Los Angeles, Los Angeles, California 90024, USA*

⁹*Instituto de Física de Cantabria, CSIC-University of Cantabria, 39005 Santander, Spain*

¹⁰*Carnegie Mellon University, Pittsburgh, Pennsylvania 15213, USA*

¹¹*Enrico Fermi Institute, University of Chicago, Chicago, Illinois 60637, USA*

¹²*Comenius University, 842 48 Bratislava, Slovakia; Institute of Experimental Physics, 040 01 Kosice, Slovakia*

¹³*Joint Institute for Nuclear Research, RU-141980 Dubna, Russia*

¹⁴*Duke University, Durham, North Carolina 27708, USA*

¹⁵*Fermi National Accelerator Laboratory, Batavia, Illinois 60510, USA*

¹⁶*University of Florida, Gainesville, Florida 32611, USA*

¹⁷*Laboratori Nazionali di Frascati, Istituto Nazionale di Fisica Nucleare, I-00044 Frascati, Italy*

¹⁸*University of Geneva, CH-1211 Geneva 4, Switzerland*

¹⁹*Glasgow University, Glasgow G12 8QQ, United Kingdom*

²⁰*Harvard University, Cambridge, Massachusetts 02138, USA*

²¹*Division of High Energy Physics, Department of Physics,*

University of Helsinki and Helsinki Institute of Physics, FIN-00014, Helsinki, Finland

²²*University of Illinois, Urbana, Illinois 61801, USA*

²³*The Johns Hopkins University, Baltimore, Maryland 21218, USA*

²⁴*Institut für Experimentelle Kernphysik, Karlsruhe Institute of Technology, D-76131 Karlsruhe, Germany*

²⁵*Center for High Energy Physics: Kyungpook National University,*

Daegu 702-701, Korea; Seoul National University, Seoul 151-742,

Korea; Sungkyunkwan University, Suwon 440-746,

Korea; Korea Institute of Science and Technology Information,

[†] With visitors from ^aIstituto Nazionale di Fisica Nucleare, Sezione di Cagliari, 09042 Monserrato (Cagliari), Italy, ^bUniversity of CA Irvine, Irvine, CA 92697, USA, ^cUniversity of CA Santa Barbara, Santa Barbara, CA 93106, USA, ^dUniversity of CA Santa Cruz, Santa Cruz, CA 95064, USA, ^eInstitute of Physics, Academy of Sciences of the Czech Republic, Czech Republic, ^fCERN, CH-1211 Geneva, Switzerland, ^gCornell University, Ithaca, NY 14853, USA, ^hUniversity of Cyprus, Nicosia CY-1678, Cyprus, ⁱOffice of Science, U.S. Department of Energy, Washington, DC 20585, USA, ^jUniversity College Dublin, Dublin 4, Ireland, ^kETH, 8092 Zurich, Switzerland, ^lUniversity of Fukui, Fukui City, Fukui Prefecture, Japan 910-0017, ^mUniversidad Iberoamericana, Mexico D.F., Mexico, ⁿUniversity of Iowa, Iowa City, IA 52242, USA, ^oKinki University, Higashi-Osaka City, Japan 577-8502, ^pKansas State University, Manhattan, KS 66506, USA, ^qKorea University, Seoul, 136-713, Korea, ^rUniversity of Manchester, Manchester M13 9PL, United Kingdom, ^sQueen Mary, University of London, London, E1 4NS, United Kingdom, ^tUniversity of Melbourne, Victoria 3010, Australia, ^uMuons, Inc., Batavia, IL 60510, USA, ^vNagasaki Institute of Applied Science, Nagasaki, Japan, ^wNational Research Nuclear University, Moscow, Russia, ^xNorthwestern University, Evanston, IL 60208, USA, ^yUniversity of Notre Dame, Notre Dame, IN 46556, USA, ^zUniversidad de Oviedo, E-33007 Oviedo, Spain, ^{aa}CNRS-IN2P3, Paris, F-75205 France, ^{bb}Texas Tech University, Lubbock, TX 79609, USA, ^{cc}Universidad Tecnica Federico Santa Maria, 110v Valparaiso, Chile, ^{dd}Yarmouk University, Irbid 211-63, Jordan,

- Daejeon 305-806, Korea; Chonnam National University, Gwangju 500-757, Korea; Chonbuk National University, Jeonju 561-756, Korea
- ²⁶Ernest Orlando Lawrence Berkeley National Laboratory, Berkeley, California 94720, USA
- ²⁷University of Liverpool, Liverpool L69 7ZE, United Kingdom
- ²⁸University College London, London WC1E 6BT, United Kingdom
- ²⁹Centro de Investigaciones Energeticas Medioambientales y Tecnologicas, E-28040 Madrid, Spain
- ³⁰Massachusetts Institute of Technology, Cambridge, Massachusetts 02139, USA
- ³¹Institute of Particle Physics: McGill University, Montréal, Québec, Canada H3A 2T8; Simon Fraser University, Burnaby, British Columbia, Canada V5A 1S6; University of Toronto, Toronto, Ontario, Canada M5S 1A7; and TRIUMF, Vancouver, British Columbia, Canada V6T 2A3
- ³²University of Michigan, Ann Arbor, Michigan 48109, USA
- ³³Michigan State University, East Lansing, Michigan 48824, USA
- ³⁴Institution for Theoretical and Experimental Physics, ITEP, Moscow 117259, Russia
- ³⁵University of New Mexico, Albuquerque, New Mexico 87131, USA
- ³⁶The Ohio State University, Columbus, Ohio 43210, USA
- ³⁷Okayama University, Okayama 700-8530, Japan
- ³⁸Osaka City University, Osaka 588, Japan
- ³⁹University of Oxford, Oxford OX1 3RH, United Kingdom
- ⁴⁰Istituto Nazionale di Fisica Nucleare, Sezione di Padova-Trento, ^{fj}University of Padova, I-35131 Padova, Italy
- ⁴¹University of Pennsylvania, Philadelphia, Pennsylvania 19104, USA
- ⁴²Istituto Nazionale di Fisica Nucleare Pisa, ^{gg}University of Pisa, ^{hh}University of Siena and ⁱⁱScuola Normale Superiore, I-56127 Pisa, Italy
- ⁴³University of Pittsburgh, Pittsburgh, Pennsylvania 15260, USA
- ⁴⁴Purdue University, West Lafayette, Indiana 47907, USA
- ⁴⁵University of Rochester, Rochester, New York 14627, USA
- ⁴⁶The Rockefeller University, New York, New York 10065, USA
- ⁴⁷Istituto Nazionale di Fisica Nucleare, Sezione di Roma 1, ^{jj}Sapienza Università di Roma, I-00185 Roma, Italy
- ⁴⁸Rutgers University, Piscataway, New Jersey 08855, USA
- ⁴⁹Texas A&M University, College Station, Texas 77843, USA
- ⁵⁰Istituto Nazionale di Fisica Nucleare Trieste/Udine, I-34100 Trieste, ^{kk}University of Udine, I-33100 Udine, Italy
- ⁵¹University of Tsukuba, Tsukuba, Ibaraki 305, Japan
- ⁵²Tufts University, Medford, Massachusetts 02155, USA
- ⁵³University of Virginia, Charlottesville, Virginia 22906, USA
- ⁵⁴Waseda University, Tokyo 169, Japan
- ⁵⁵Wayne State University, Detroit, Michigan 48201, USA
- ⁵⁶University of Wisconsin, Madison, Wisconsin 53706, USA
- ⁵⁷Yale University, New Haven, Connecticut 06520, USA
- (Dated: October 9, 2018)

We report measurements of the inclusive transverse momentum (p_T) distribution of centrally produced K_S^0 , $K^{*\pm}(892)$, and $\phi^0(1020)$ mesons up to $p_T = 10$ GeV/ c in minimum-bias events, and K_S^0 and Λ^0 particles up to $p_T = 20$ GeV/ c in jets with transverse energy between 25 GeV and 160 GeV in $p\bar{p}$ collisions. The data were taken with the CDF II detector at the Fermilab Tevatron at $\sqrt{s} = 1.96$ TeV. We find that as p_T increases, the p_T slopes of the three mesons (K_S^0 , $K^{*\pm}$, and ϕ) are similar, and the ratio of Λ^0 to K_S^0 as a function of p_T in minimum-bias events becomes similar to the fairly constant ratio in jets at $p_T \sim 5$ GeV/ c . This suggests that the particles with $p_T \gtrsim 5$ GeV/ c in minimum-bias events are from “soft” jets, and that the p_T slope of particles in jets is insensitive to light quark flavor (u , d , or s) and to the number of valence quarks. We also find that for $p_T \lesssim 4$ GeV relatively more Λ^0 baryons are produced in minimum-bias events than in jets.

PACS numbers: 13.85.Ni, 13.85.Qk, 13.87.Fh, 14.40.Df

I. INTRODUCTION

The study of particles with low p_T (transverse momentum with respect to the beam direction) from hadron-hadron interactions is as old as high energy physics itself. Nevertheless, attempts to understand the physics of particle production have had limited success. As the center-of-mass energy increases, the number of produced particles increases and events get more complex. Although the discovery of high transverse energy, E_T , jets in hadron collisions at the CERN ISR [1] and $S\bar{p}\bar{p}S$ Collider [2] supported the theory of strongly interacting quarks and gluons (QCD), low

p_T hadron production is still not well understood despite additional data from $p\bar{p}$ and pp colliders including RHIC [3] because the strong coupling is large, and perturbative QCD calculations do not apply. Phenomenological models, such as PYTHIA [4], have been developed and tuned to data. New data, such as that presented here on strange particle production, can further refine the models.

Hadron-hadron collisions are classified into two types, elastic and inelastic collisions. Inelastic hadron-hadron collisions are generally further classified as diffractive and non-diffractive. The diffractive events have a large rapidity gap (> 3) with no hadrons. The distinction is not absolute, and experiments (and theorists) should make their definitions explicit.

Inelastic collisions can have a hard parton-parton interaction resulting in high E_T jets, and we select events with jets with E_T from 25 to 160 GeV and measure the production of hadrons with strange quarks in the jets. In this paper, we present the invariant differential cross section, $Ed^3\sigma/dp^3$, of K_S^0 , $K^{*\pm}$, and ϕ particles up to $p_T = 10$ GeV/c in typical non-diffractive events, and the p_T distributions of K_S^0 and Λ^0 in jets up to $p_T = 20$ GeV/c and jet $E_T = 160$ GeV. This is the first time that the p_T distributions of identified particles in high- E_T jets from hadron-hadron collisions have been measured. These spectra extend down to $p_T \sim 1$ GeV/c where perturbative calculations cannot be used. The various phenomenological approaches in this region (some inspired by QCD) benefit from such data.

One goal of this analysis is to compare particle production from minimum-bias (MB) and jet events to see if there is a transition at some p_T , above which the particles from jet fragmentation tend to dominate. Another goal is to test the fragmentation process of quarks and gluons to jets in the PYTHIA event generator tuned to e^+e^- [5] and e^-p [6] data. Because the particles are identified, the comparison can be more sensitive to details, e.g., s -quark creation. A third goal is to provide information on particles produced with p_T less than ~ 3 GeV/c in MB events. Apart from their intrinsic interest, such data are useful in searches for quark-gluon plasma signatures in heavy-ion collisions.

II. EVENT AND JET SELECTION

The data in this analysis are from the CDF II detector at the Tevatron Collider operating at a center-of-mass energy $\sqrt{s} = 1.96$ TeV. The CDF II detector was described in detail elsewhere [7]. The components most relevant to this analysis are the tracking system and the calorimeters. The tracking system was in a uniform axial magnetic field of 1.4 T. The inner tracker had seven to eight layers of silicon microstrip detectors ranging in radius from 1.5 to 28.0 cm [8] in the pseudorapidity region $|\eta| < 2$ [9]. Outside this was the Central Outer Tracker (COT) a cylindrical drift chamber with 96 sense-wire layers grouped in eight superlayers of axial and stereo wires [10]. Its active volume covered 40 to 140 cm in radius and $|z| < 155$ cm, where z is the coordinate along the beam direction centered in the middle of the detector.

Surrounding the tracking system were the pointing-tower-geometry electromagnetic (EM) and hadronic calorimeters [11], divided into central ($|\eta| < 1.1$) and plug ($1.1 < |\eta| < 3.6$) regions. The calorimeters were made of lead (EM) and iron (hadronic) absorbers sandwiched between plastic scintillators that provided measurements of shower energies. At a depth approximately corresponding to the maximum development of the typical electromagnetic shower, the EM calorimeters contained proportional chambers [12] to measure shower positions and profiles.

MB events were collected with a trigger selecting beam-bunch crossings with at least one inelastic $p\bar{p}$ interaction. We required a time coincidence between signals in both forward and backward gas Cherenkov counters [13] covering the regions $3.7 < |\eta| < 4.7$. In these events we study K_S^0 , $K^{*\pm}$, and ϕ production in the central region, $|\eta| < 1.0$.

The high- E_T jet events were collected with four jet transverse-energy trigger thresholds: 20, 50, 70, and 100 GeV, and the lower E_T threshold events were randomly accepted at a fixed fraction in order to reduce the trigger rate. Jets are constructed using a fixed-cone algorithm with radius $\Delta R = \sqrt{(\Delta\eta)^2 + (\Delta\phi)^2} = 0.4$, and their energies are corrected for detector effects [14]. Jets with $|\eta| < 1.0$ are used and these jets are divided into five E_T ranges: 25 – 40 GeV, 40 – 60 GeV, 60 – 80 GeV, 80 – 120 GeV and 120 – 160 GeV. We study the production properties of K_S^0 and Λ^0 for each range.

We require a reconstructed event vertex in the fiducial region $|z_{\text{VTX}}| \leq 60$ cm. Tracks are required to have a high track-fit quality, with χ^2 per degree-of-freedom (χ^2/dof) ≤ 2.5 , with more than five hits in at least two axial and two stereo COT track segments reconstructed in superlayers. It is further required that tracks have $|\eta| < 1$ and $p_T > p_T^{\text{min}}$, where $p_T^{\text{min}} = 0.325$ GeV/c and 0.5 GeV/c for MB events and jet events respectively.

III. K_S^0 AND Λ^0 RECONSTRUCTION

The K_S^0 and Λ^0 reconstruction procedures are similar. Since the Λ^0 reconstruction is well described in a previous publication [15], a summary for K_S^0 reconstruction is presented here. We search for K_S^0 to $\pi^+\pi^-$ decays using tracks with opposite charge and $p_T > p_T^{\text{min}}$ that satisfy the χ^2/dof and COT segment requirements.

For each track pair we calculate the position of their intersection in the transverse ($r-\phi$) plane. Once this intersection point, referred to as the secondary vertex, is found, the z -coordinate of each track (z_1 and z_2) is calculated at that point. If the distance $|z_1 - z_2|$ is less than 1.5 cm, the tracks are considered to originate from a K_S^0 candidate decay. The pair is traced back to the primary event vertex and we require δz_0 to be less than 2 cm, and d_0 to be less than 0.25 cm. The quantities δz_0 and d_0 are the distances between the event vertex and the track position at the point of closest approach to the event vertex in the z -axis and in the $r-\phi$ plane respectively. To further reduce the background, we require the K_S^0 transverse-decay length $L_{K_S^0}$, the distance in the $r-\phi$ plane between the primary and secondary vertices, to be $2.5 < L_{K_S^0} < 50$ cm. The Λ^0 selection criteria are the same as K_S^0 except for the lower limit of the decay length requirement, which is 5 cm. The invariant mass of the two-track system is calculated by attributing the charged-pion mass to both tracks. The left plot in Fig. 1 shows the $\pi^+\pi^-$ invariant mass ($M_{\pi^+\pi^-}$) for K_S^0 candidates with $|\eta| < 1$ in MB events. For the Λ^0 reconstruction, the track with the higher momentum is assigned the proton mass. Any reference to Λ^0 implies $\bar{\Lambda}^0$ as well. The invariant mass distributions are modeled with either a Gaussian or Breit-Wigner function for the signal and a third-degree polynomial function for the background. As the widths of particles are small, the third-degree polynomial is adequate to model the background shape within the fit range.

IV. $K^{*\pm}$ AND ϕ RECONSTRUCTION

$K^{*\pm}$ and ϕ particles are only reconstructed in MB events. We reconstruct $K^{*\pm}$ decaying into K_S^0 and π^\pm . Since the lifetime of $K^{*\pm}$ is very short, the reconstructed K_S^0 candidates from the previous section with their mass $0.47 < M_{\pi^+\pi^-} < 0.53$ GeV/c^2 and a track with $p_T > 0.325$ GeV/c are combined at the event vertex. For both the K_S^0 candidate and the track, we require that the impact parameter d_0 to be less than 0.25 cm, and δz_0 to be less than 2 cm. The charged-pion mass is assigned to the track. The center plot in Fig. 1 shows the invariant mass of a K_S^0 and a charged pion combinations ($M_{K_S^0\pi^\pm}$), and there is a distinct $K^{*\pm}$ signal.

The final state for ϕ reconstruction is K^+ and K^- . Since the lifetime of ϕ is also very short, two oppositely-charged tracks, assumed to be kaons, with $p_T > 0.325$ GeV/c , are combined at the event vertex after requiring $d_0 < 0.25$ cm and $\delta z_0 < 2$ cm for both tracks. The right plot in Fig. 1 shows the two-kaon invariant mass ($M_{K^+K^-}$) after the same sign KK invariant mass distribution is subtracted. There is a mismatch between the data and the fitted curve near $M_{K^+K^-} \sim 1.03$ GeV/c^2 at the level of a few percentage of the signal events, much less than the systematic uncertainty due to the fitting procedure as discussed later.

To measure the p_T cross-section distribution of a resonance, the data in the invariant mass distribution are divided into many p_T intervals and the number of resonances is calculated for each p_T interval from a fit to the invariant mass distribution. The numbers as a function of p_T are acceptance-corrected to produce the p_T distribution. In this paper, the word resonance is loosely used for both short-lived and long-lived particles.

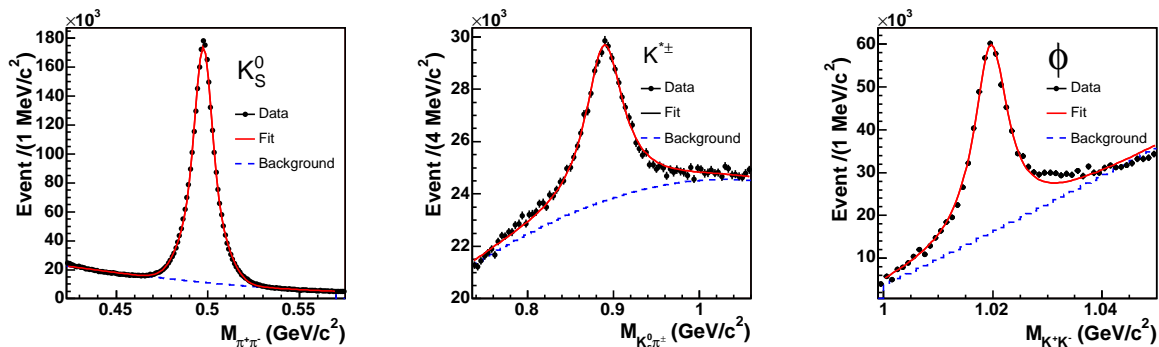


FIG. 1: Reconstructed invariant mass distributions for charged-pion pairs ($M_{\pi^+\pi^-}$), K_S^0 and pion pairs ($M_{K_S^0\pi^\pm}$) and charged-kaon pairs ($M_{K^+K^-}$) from MB events. The solid line is the fitted curve, a third-degree polynomial for the background and a double Gaussian (K_S^0) or Breit-Wigner ($K^{*\pm}$ and ϕ) function to model the signal. The widths are consistent with the mass resolution from the Monte Carlo simulation.

V. p_T DISTRIBUTIONS OF K_S^0 , $K^{*\pm}$ AND ϕ MESONS IN MB EVENTS

A. ACCEPTANCE CALCULATION AND SYSTEMATIC UNCERTAINTIES

The geometric and kinematic acceptance is estimated with Monte Carlo (MC) simulations. Each resonance state is generated with ~ 14 fixed p_T values ranging from 0.5 to 10 GeV/c and uniform in rapidity for $|y| < 2$. A generated resonance is combined with either one or four non-diffractive inelastic MB events generated with the PYTHIA generator. Although the average number of interactions in our data sample is a little less than two, the default acceptance is calculated from the MC sample with four MB events and the difference of the acceptance values between the two samples is taken as a systematic uncertainty. This is because PYTHIA underestimates the average event multiplicity.

The detector response to particles produced in the event generator is modeled with the CDF II detector simulation based on the GEANT-3 MC program [16]. Simulated events are processed and selected with the same analysis code as that used for the data. The acceptance is defined as the ratio of the number of reconstructed resonances with the input p_T divided by the generated number, including the branching ratio. Acceptance values are calculated separately for the particles and their corresponding antiparticles and the average of the two is used as the default value, since the acceptances for the two states are similar. Figure 2 shows the acceptances including the relevant branching ratios for the three particles.

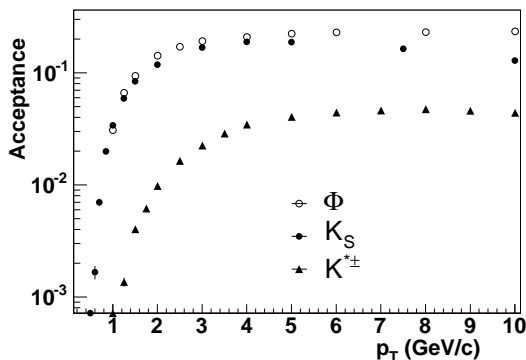


FIG. 2: Acceptance as a function of p_T for K_S^0 , $K^{*\pm}$ and ϕ mesons in MB events. The values include the branching ratios to the final states detected.

The acceptance values as a function of p_T are fitted with a fourth-degree polynomial function and the fitted curve is used to correct the numbers of each resonance state in the data. The modeling of the MB events overlapping with the resonance, and the selection criteria applied, contribute to the systematic uncertainty on the acceptance calculation. Acceptance uncertainties due to the selection criteria are studied by changing the selection values of the variables used to reconstruct the resonances. The variables examined are p_T , $|z_1 - z_2|$, δz_0 , d_0 , and the decay lengths. For each variable other than p_T , two values around the default value are typically chosen. One value is such that it has little effect on the signal, and the other reduces the signal by approximately 20 to 30%. The default minimum p_T selection value is 0.325 GeV/c, which is changed to 0.3 GeV/c and to 0.35 GeV/c.

For each considered variation, a new acceptance curve and number of resonances as a function of p_T are obtained, and the percentage change between the new p_T distribution and that with the default selection requirements is taken as the uncertainty in the acceptance for the specific p_T interval. The sum in quadrature of all variations is taken as the total uncertainty on the acceptance in a given p_T bin. For the K_S^0 case, the acceptance uncertainty decreases from about 15% at $p_T \sim 1$ GeV/c to 4% at $p_T \sim 5$ GeV/c and then rises again to 10% at $p_T = 10$ GeV/c. This acceptance uncertainty is added quadratically to the systematic uncertainty due to the fitting procedure, described later, to give the total systematic uncertainty.

For $K^{*\pm}$ and ϕ mesons the examined variables are p_T , δz_0 and d_0 as they decay at the event vertex. The acceptance uncertainty for the $K^{*\pm}$ case decreases from about 25% at $p_T \sim 1.5$ GeV/c to 10% at $p_T \sim 5$ GeV/c and then rises to $\sim 15\%$ at 10 GeV/c. For the ϕ meson, the uncertainty decreases from about 15% at $p_T \sim 1$ GeV/c to 10% at $p_T \sim 2$ GeV/c, decreases to 6% at $p_T \sim 5$ GeV/c and is then constant.

B. p_T DISTRIBUTIONS

The first step to get the p_T distribution is to calculate the number of resonances as a function of p_T from the invariant mass plots. The data in the invariant mass plot for each resonance are divided into many p_T intervals. The number of p_T intervals depends on the resonance type and is dictated by statistics such that the fits to the invariant mass distributions are stable. The number of resonances in each p_T interval is determined by fitting the invariant mass distributions using a Gaussian (K_S^0) or non-relativistic Breit-Wigner ($K^{*\pm}$ and ϕ) function with three parameters for the signal, and a third-degree polynomial for the underlying background. The measured mass distributions of the $K^{*\pm}$ and ϕ are not exactly a Breit-Wigner shape because of the detector resolution. The detector effect on the mass shape is treated as one of the systematic uncertainties. The polynomial fit to the background is subtracted bin-by-bin from the data in the mass interval to obtain the number of resonances. This number is divided by the acceptance to obtain the p_T cross-section distributions. Table I shows the mass intervals for each resonance.

The fitting procedure is one source of systematic uncertainty. This uncertainty is estimated by separately varying the mass range of the fit, the functional form for the signal to a double Gaussian function (K_S^0) or a Breit-Wigner function convoluted with a Gaussian ($K^{*\pm}$ and ϕ), and the background modeling function to a second-order polynomial. The mass and width of the Breit-Wigner function are fixed to the values in the Review of Particle Properties [17]. The number of signal events is recalculated in all p_T intervals for each variation. The systematic uncertainty is determined as the sum in quadrature of the fractional change in the number of signal events from each modified fit. Because the K_S^0 signals are clearly visible, the systematic uncertainty is low, less than 5% up to $p_T = 10$ GeV/ c . For the $K^{*\pm}$ case it decreases from about 25% at $p_T \sim 1$ GeV/ c to 6% at $p_T \sim 4$ GeV/ c and then rises to $\sim 10\%$ at 10 GeV/ c . For the ϕ meson, the uncertainty decreases from about 25% at $p_T \sim 1$ GeV/ c to 8% for $p_T > 2$ GeV/ c and remains fairly constant. The high uncertainty in the low p_T region is due to a large combinatorial background. The total systematic uncertainty is the square root of the quadratic sum of the fitting uncertainty in this section and the uncertainty in the acceptance calculation.

TABLE I: The mass intervals used to select the signal events. The polynomial fit to the background is subtracted bin-by-bin from the data in the mass interval to obtain the number of signal events. The unit is GeV/ c^2 .

Particle type	MB events	Jet events
Λ^0	-	1.105 – 1.132
K_S^0	0.48 – 0.516	0.465 – 0.535
$K^{*\pm}$	0.841 – 0.943	-
ϕ	1.01 – 1.03	-

The inclusive invariant differential cross section as a function of p_T for each particle within $|\eta| < 1$ is calculated as $E d^3\sigma/dp^3 = (\sigma_{\text{mb}}/N_{\text{event}})d^3N/Ap_T dp_T dy d\phi = (\sigma_{\text{mb}}/2\pi N_{\text{event}})\Delta N/Ap_T \Delta p_T \Delta y$ where σ_{mb} is the MB cross section 45 ± 8 mb [18] passing our trigger requirement, N_{event} is the number of events, ΔN is the number of resonances observed in each p_T interval (Δp_T) after the background subtraction, A is the acceptance in the specific p_T interval, and Δy is the rapidity range used in the acceptance calculation ($-2 < y < 2$).

Figure 3 shows the results for the differential cross sections as a function of p_T for the three resonances. The uncertainties shown for each data point include the statistical and all systematic uncertainties described above, except for that associated with σ_{mb} [18]. The systematic uncertainties of data points neighboring a p_T value are correlated because the decay kinematics of the daughter particles are similar. The cross sections in Fig. 3 are listed in Table II. The displayed p_T values are the weighted averages within the p_T intervals based on the cross section calculated from the fit parameters described below.

The p_T differential cross section is modeled by a power law function, $A(p_0)^n/(p_T + p_0)^n$, for $p_T > 2$ GeV/ c . In order to compare with the previous publications on hyperons (Λ , Ξ , and Ω) [15], p_0 is fixed at 1.3 GeV/ c , and the results are shown in Table III. Compared to hyperons, the values of the parameter n for mesons are lower by $\sim 10\%$. The data below $p_T \sim 2$ GeV/ c cannot be described well by the power law function even if p_0 is allowed to float. For this region, the data are better described by an exponential function, $Be^{-b \cdot p_T}$. The p_T ranges and results of this fit are shown in Table IV, and the slope b of ϕ is consistent with a previous measurement [24]. The b values depend on the range of the fit.

Figure 4 shows the p_T differential cross section ratios of $K^{*\pm}$ to K_S^0 and ϕ to K_S^0 . The K_S^0 cross section is multiplied by two to account for the K_L^0 production. The $K^{*\pm}$ to K_S^0 ratio increases as p_T increases, reaches a plateau at ~ 5 GeV/ c p_T and stays flat. The rise in the ϕ to K_S^0 ratio at low p_T is slower than the $K^{*\pm}$ to K_S^0 ratio and reaches the plateau at an earlier p_T . The two ratios as a function of p_T exhibit a similar behavior as $\Xi^\pm/(\Lambda^0 + \bar{\Lambda}^0)$ and $\Omega^\pm/(\Lambda^0 + \bar{\Lambda}^0)$ [15].

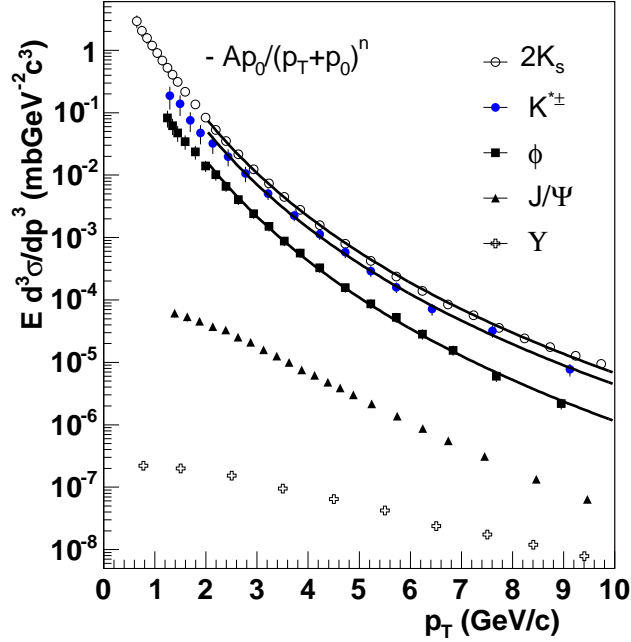


FIG. 3: The inclusive invariant p_T differential cross section distributions ($E d^3 \sigma / dp^3$) for K_S^0 , $K^{*\pm}$, and ϕ within $|\eta| < 1$. The K_S^0 cross section is multiplied by two to take K_L^0 production into account. The solid curves are from fits to a power law function, with the fitted parameters given in Table III. The J/Ψ [20] and Υ [21] data are shown for comparison.

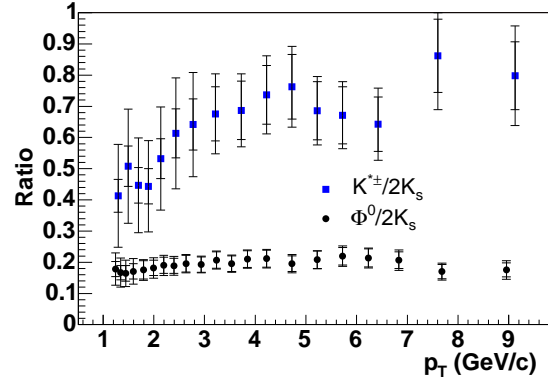


FIG. 4: The cross-section ratios as a function of p_T of $K^{*\pm}$ to K_S^0 and ϕ to K_S^0 . The K_S^0 cross section is multiplied by 2. There are two error bars for each data point. The inner (outer) one corresponds to the statistical (systematic) uncertainty.

In Figure 5, the differential cross sections of the three resonances are compared with PYTHIA events generated with default parameters. The ϕ cross section matches well while PYTHIA K_S^0 ($K^{*\pm}$) cross section is somewhat lower (higher) than the data. The PYTHIA parameters responsible for the strange meson production cross sections were varied [23] but it was not possible to produce a good match for all three resonances.

TABLE II: The inclusive invariant differential cross section values for K_S^0 , ϕ , and $K^{*\pm}$ mesons in Fig. 3. The uncertainties include both the statistical and systematic uncertainties added in quadrature but do not include σ_{mb} uncertainty.

p_T (GeV/c)	$2K_S^0$ ($mb \text{ GeV}^{-2} c^3$)	p_T	ϕ	p_T	$K^{*\pm}$
.645	2.94 ± 0.66	1.24	$(8.25 \pm 2.48) \times 10^{-2}$	1.29	$(1.87 \pm 0.74) \times 10^{-1}$
.745	2.05 ± 0.43	1.34	$(6.17 \pm 1.80) \times 10^{-2}$	1.49	$(1.39 \pm 0.51) \times 10^{-1}$
.845	1.58 ± 0.30	1.44	$(4.75 \pm 1.34) \times 10^{-2}$	1.69	$(7.56 \pm 2.63) \times 10^{-2}$
.945	1.19 ± 0.22	1.59	$(3.45 \pm 0.91) \times 10^{-2}$	1.90	$(4.72 \pm 1.60) \times 10^{-2}$
1.04	$(9.09 \pm 1.58) \times 10^{-1}$	1.79	$(2.36 \pm 0.58) \times 10^{-2}$	2.13	$(3.21 \pm 1.02) \times 10^{-2}$
1.15	$(6.88 \pm 1.15) \times 10^{-1}$	1.99	$(1.41 \pm 0.29) \times 10^{-2}$	2.44	$(1.98 \pm 0.60) \times 10^{-2}$
1.24	$(5.25 \pm 0.84) \times 10^{-1}$	2.19	$(1.01 \pm 0.20) \times 10^{-2}$	2.77	$(1.06 \pm 0.29) \times 10^{-2}$
1.34	$(4.06 \pm 0.63) \times 10^{-1}$	2.40	$(6.61 \pm 1.23) \times 10^{-3}$	3.21	$(5.06 \pm 1.07) \times 10^{-3}$
1.44	$(3.13 \pm 0.48) \times 10^{-1}$	2.63	$(4.03 \pm 0.72) \times 10^{-3}$	3.73	$(2.25 \pm 0.44) \times 10^{-3}$
1.59	$(2.17 \pm 0.32) \times 10^{-1}$	2.94	$(2.40 \pm 0.41) \times 10^{-3}$	4.22	$(1.13 \pm 0.22) \times 10^{-3}$
1.79	$(1.35 \pm 0.19) \times 10^{-1}$	3.23	$(1.51 \pm 0.26) \times 10^{-3}$	4.72	$(5.80 \pm 1.13) \times 10^{-4}$
1.99	$(8.37 \pm 1.14) \times 10^{-2}$	3.54	$(8.73 \pm 1.49) \times 10^{-4}$	5.22	$(2.90 \pm 0.56) \times 10^{-4}$
2.19	$(5.32 \pm 0.71) \times 10^{-2}$	3.84	$(5.67 \pm 0.97) \times 10^{-4}$	5.72	$(1.60 \pm 0.31) \times 10^{-4}$
2.40	$(3.53 \pm 0.46) \times 10^{-2}$	4.22	$(3.26 \pm 0.56) \times 10^{-4}$	6.42	$(7.16 \pm 1.51) \times 10^{-5}$
2.63	$(2.17 \pm 0.28) \times 10^{-2}$	4.72	$(1.57 \pm 0.27) \times 10^{-4}$	7.61	$(3.21 \pm 0.73) \times 10^{-5}$
2.94	$(1.24 \pm 0.16) \times 10^{-2}$	5.22	$(8.69 \pm 1.55) \times 10^{-5}$	9.13	$(7.70 \pm 1.76) \times 10^{-6}$
3.23	$(7.33 \pm 0.96) \times 10^{-3}$	5.72	$(5.25 \pm 0.94) \times 10^{-5}$	-	-
3.54	$(4.50 \pm 0.59) \times 10^{-3}$	6.24	$(2.84 \pm 0.53) \times 10^{-5}$	-	-
3.84	$(2.78 \pm 0.36) \times 10^{-3}$	6.83	$(1.56 \pm 0.29) \times 10^{-5}$	-	-
4.22	$(1.57 \pm 0.20) \times 10^{-3}$	7.68	$(6.01 \pm 1.17) \times 10^{-6}$	-	-
4.72	$(7.91 \pm 1.03) \times 10^{-4}$	8.96	$(2.18 \pm 0.42) \times 10^{-6}$	-	-
5.22	$(4.22 \pm 0.55) \times 10^{-4}$	-	-	-	-
5.72	$(2.38 \pm 0.31) \times 10^{-4}$	-	-	-	-
6.24	$(1.39 \pm 0.18) \times 10^{-4}$	-	-	-	-
6.74	$(8.46 \pm 1.10) \times 10^{-5}$	-	-	-	-
7.24	$(5.70 \pm 0.74) \times 10^{-5}$	-	-	-	-
7.74	$(3.57 \pm 0.47) \times 10^{-5}$	-	-	-	-
8.24	$(2.43 \pm 0.32) \times 10^{-5}$	-	-	-	-
8.74	$(1.75 \pm 0.23) \times 10^{-5}$	-	-	-	-
9.24	$(1.28 \pm 0.17) \times 10^{-5}$	-	-	-	-
9.74	$(9.42 \pm 1.23) \times 10^{-6}$	-	-	-	-

TABLE III: The results of power law function fits to the inclusive invariant p_T differential cross sections shown in Fig. 3 for $p_T > 2$ GeV/c. The parameter p_0 is fixed to 1.3 GeV/c in all fits. K_S^0 results are without the scale factor two which takes into account the K_L^0 meson. The K_S^0 values in the second column are from $\sqrt{s} = 1.8$ TeV [22]. The uncertainties do not include σ_{mb} uncertainty. The last line of the table gives the χ^2 per degree-of-freedom of the fit to data.

Fit parameter (units)	K_S^0 [Run I]	K_S^0	$K^{*\pm}$	ϕ
A ($mb \text{ GeV}^{-2} c^3$)	45 ± 9	50.2 ± 6.1	60.4 ± 13.5	23.5 ± 2.55
p_0 (GeV/c)	1.3	1.3	1.3	1.3
n	7.7 ± 0.2	7.65 ± 0.08	7.60 ± 0.19	7.80 ± 0.80
χ^2/dof	8.1/11	6.0/17	3.9/10	14.0/13

TABLE IV: The results of exponential function fits to the inclusive invariant p_T differential cross sections shown in Fig. 3 for the p_T ranges given in the second row. The K_S^0 results are without the scale factor two which takes into account the K_L^0 meson. The uncertainties shown do not include σ_{mb} uncertainty. The last line of the table gives the χ^2 per degree-of-freedom of the fit to data.

Fit parameter (units)	K_S^0	K_S^0	K_S^0	$K^{*\pm}$	ϕ
p_T range (GeV/c)	[0.6, 1.5]	[0.6, 2.5]	[1.2, 2.5]	[1.2, 2.5]	[1.2, 2.5]
B ($mb \text{ GeV}^{-2} c^3$)	10.4 ± 2.4	6.55 ± 0.80	5.00 ± 0.92	1.79 ± 1.203	1.20 ± 0.40
b ($\text{GeV}^{-1} c$)	3.02 ± 0.20	2.60 ± 0.08	2.41 ± 0.10	2.01 ± 0.35	2.20 ± 0.18
χ^2/dof	1.0/9	7.2/12	0.7/6	0.8/4	0.3/7

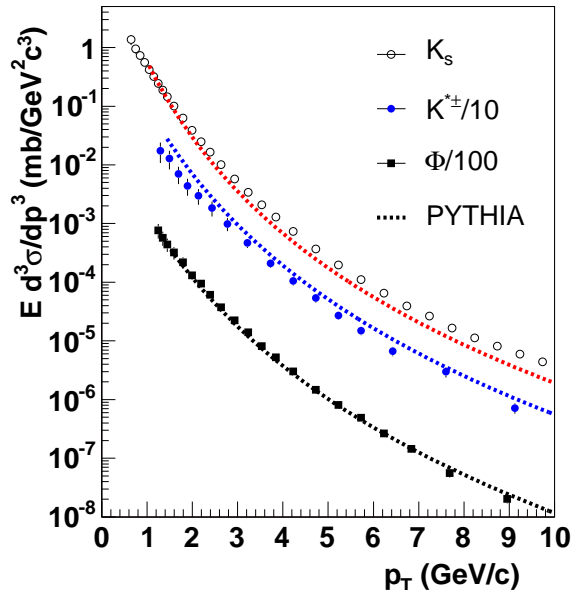


FIG. 5: The inclusive invariant p_T differential cross section distributions in Fig. 3 are compared with PYTHIA version 6 with default parameters. The $K^{*\pm}$ (ϕ) cross section is divided by 10 (100).

VI. p_T DISTRIBUTIONS OF K_S^0 AND Λ^0 HADRONS IN JETS

A. ACCEPTANCE CALCULATION AND SYSTEMATIC UNCERTAINTIES

For jet events, K_S^0 and Λ^0 candidates reconstructed as previously discussed are divided into five jet- E_T ranges. A candidate is assigned to a jet if $\Delta R < 0.5$, where ΔR is the distance between the resonance and jet in the $\eta - \phi$ plane. If the candidate belongs to more than one jet, it is associated to the nearest jet. The ΔR range 0.5 is slightly larger than the 0.4 used in the jet clustering to include low p_T resonances. Figure 6 shows $M_{\pi^+\pi^-}$ distributions from jets with $60 < E_T < 80$ GeV and Fig. 7 shows the same but for the $M_{p\pi^-} + M_{\bar{p}\pi^+}$ distributions. Because at large p_T the Λ^0 signal becomes unclear (bottom right plot in Fig. 7), the Λ^0 data with $p_T > 15$ GeV/c and jet $E_T > 60$ GeV are not used.

The acceptance for K_S^0 and Λ^0 hadrons in jets as a function of p_T is calculated for each jet- E_T interval and defined as the ratio of the number of reconstructed resonances to the number of generated resonances in the jets. The acceptances in jets are calculated using the QCD jet events generated with PYTHIA, passed through the CDF II detector simulation, and reconstructed. A jet event is mixed with one or four PYTHIA inelastic MB events. The default acceptance is calculated with the sample mixed with four MB events, and the difference of the acceptance values between the two samples is one of our systematic uncertainties, as in the case of MB events.

We select the generated resonances in the MC data with $\Delta R < 0.5$ where ΔR is measured with respect to the reconstructed jet direction. We also select the reconstructed resonances within the same ΔR range, and mark the ones with matched generated resonances based on $|\Delta\eta| < 0.075$ and $|\Delta\phi| < 0.075$, where $\Delta\phi$ ($\Delta\eta$) is the difference in ϕ (η) between the generated and reconstructed resonances. The acceptance as a function of p_T is the ratio of the p_T distribution of the marked reconstructed resonances to the generated resonances. Figure 8 shows the K_S^0 acceptance for the five jet- E_T intervals and Fig. 9 shows the same for Λ^0 . The acceptances include the branching ratio to our final states.

The sources of systematic uncertainty in the acceptance calculation are similar to those discussed for K_S^0 in MB events, and they are calculated as functions of p_T and E_T except for one difference: The default minimum p_T selection 0.5 GeV/c is changed to 0.45 GeV/c and to 0.55 GeV/c. The dependence of the K_S^0 (Λ^0) acceptance uncertainty on p_T for different E_T ranges is quite similar. It starts at ~ 10 (15)% at 2 GeV/c and decreases to ~ 5 (7)% at 5 GeV/c and then increases approximately linearly to ~ 12 (20)% at 20 GeV/c.

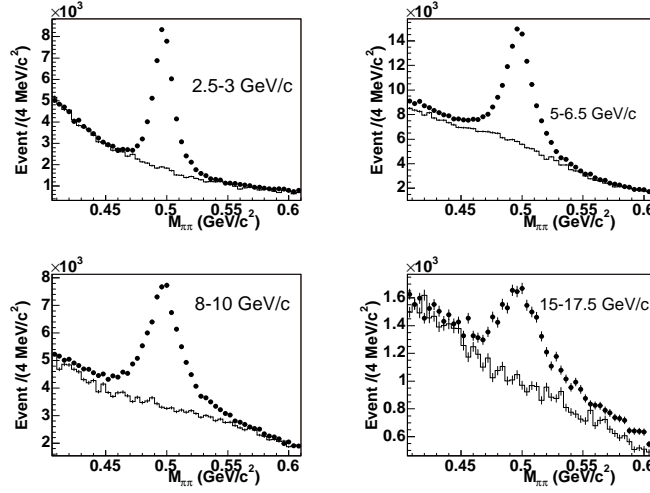


FIG. 6: Invariant $\pi^+\pi^-$ mass distributions for four p_T intervals from jets with E_T between 60 and 80 GeV. The numbers in the figures are the p_T intervals. The histograms are the background shapes called QCD-C and obtained from QCD jet simulation.

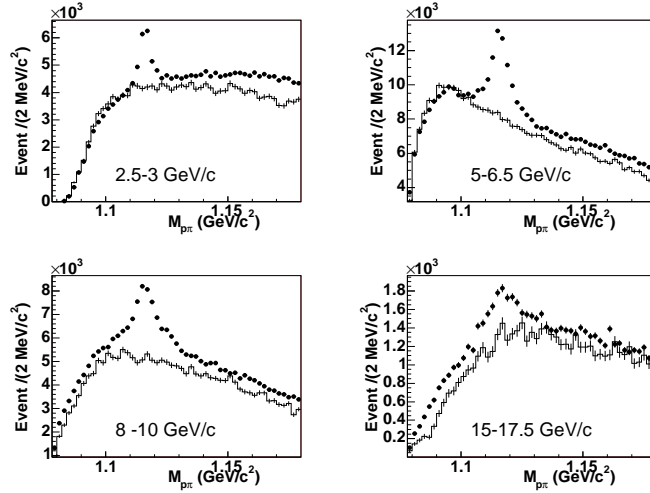


FIG. 7: Invariant $p\pi^- + \bar{p}\pi^+$ mass distributions for four p_T intervals from jets with E_T between 60 and 80 GeV. The numbers in the figures are the p_T intervals. The histograms are the background shapes called QCD-C and obtained from QCD jet simulation. Because the Λ^0 signal becomes unclear as p_T increases (bottom right plot), the data with p_T greater than 15 GeV/c and jet E_T greater than 60 GeV are not used.

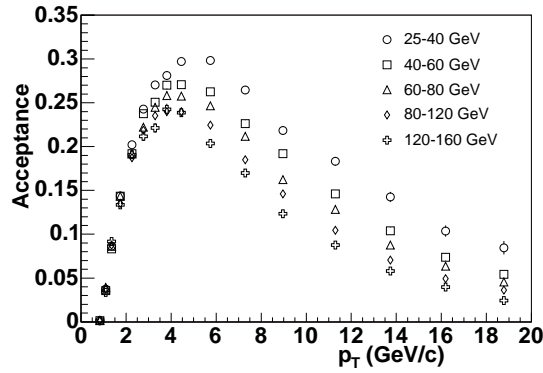


FIG. 8: K_S^0 acceptance plots for the five jet- E_T intervals. The values include the branching ratio $K_S^0 \rightarrow \pi^+\pi^-$.

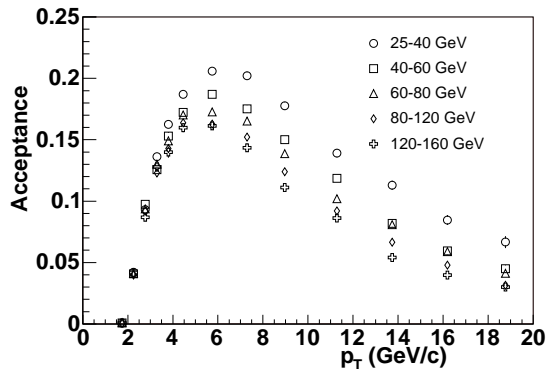


FIG. 9: Λ^0 acceptance plot for the five jet- E_T intervals. The values include the branching ratio $\Lambda^0 \rightarrow p\pi^-$.

B. p_T DISTRIBUTIONS

The measurement of the p_T distribution of particles in jets is different from that in MB events because there is more combinatorial background. We subtract the background obtained from the simulated QCD MC data sample before fitting the mass distribution. The background is called QCD combinatorial (QCD-C) background and it is the $M_{\pi\pi}$ (or $M_{p\pi}$) distribution without K_S^0 (or Λ^0).

The QCD-C background shape is obtained as follows. After choosing two tracks that form a K_S^0 (or Λ^0) candidate, we check if the candidate has a corresponding K_S^0 (or Λ^0) at the MC particle generation level in the same event by comparing the kinematic variables (ϕ and η). If the candidate has a corresponding particle at the generation level, the candidate is not entered in the invariant mass distributions and the distributions are the QCD-C backgrounds shown in Figs. 6 and 7. Disagreement with the data outside the resonance mass regions is expected since the shape of the invariant mass distribution is sensitive to the particle multiplicity and kinematics from jets. Figures 10 and 11 show the invariant mass distributions after subtracting the QCD-C backgrounds, scaled such that the entries are mostly positive after subtraction. The effect of the normalization is one of the systematic uncertainties.

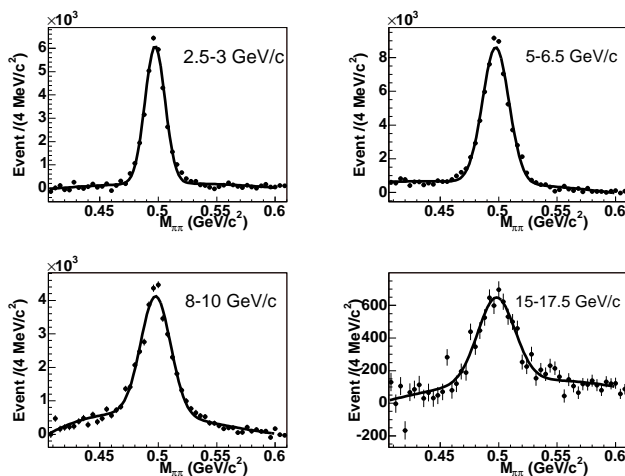


FIG. 10: Invariant $\pi^+\pi^-$ mass distributions after subtracting the scaled QCD-C background histogram from data in Fig. 6. There are four p_T intervals and the E_T of jets is between 60 and 80 GeV. The solid lines are fitted curves, a third-degree polynomial for the background and a Gaussian function with three parameters to model the K_S^0 signal.

The number of signal events in each p_T interval is determined by fitting the background-subtracted invariant mass distributions using a Gaussian function for the signal and a third-degree polynomial for the remaining background. The curves from the fits are displayed in the same figures. The polynomial function representing the background is subtracted bin-by-bin from the data in the mass interval to obtain the number of signal events. Table I shows the mass intervals. The mass intervals for jets are wider because the p_T range is extended to 20 GeV/ c and mass

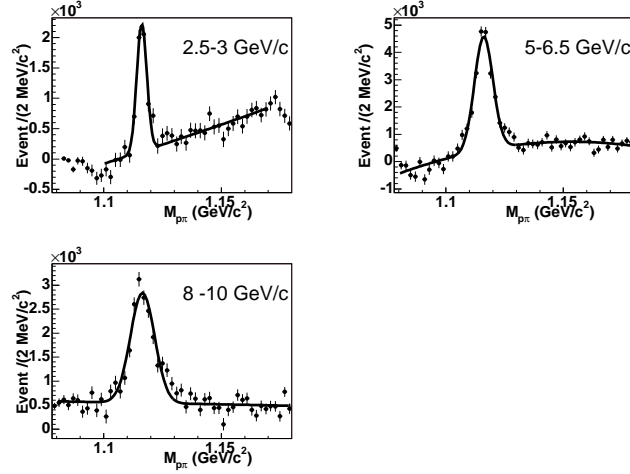


FIG. 11: Invariant $p\pi^- + \bar{p}\pi^+$ mass distributions after subtracting the scaled QCD-C background histogram from data in Fig. 7. There are three p_T intervals and E_T of jets is between 60 and 80 GeV. The solid lines are fitted curves, a third-degree polynomial for the background and a Gaussian function with three parameters to model the Λ^0 signal.

TABLE V: The K_S^0 cross-section values for the five jet- E_T intervals in Fig. 12

$p_T(\text{GeV}/c)$	$1/N_{\text{jet}}dN/(p_T dp_T) (\text{GeV}^{-2}c^2)$				
	$E_T : 25-40 \text{ GeV}$	$40-60 \text{ GeV}$	$60-80 \text{ GeV}$	$80-120 \text{ GeV}$	$120-160 \text{ GeV}$
1.75	$(2.57 \pm 0.59) \times 10^{-2}$	$(2.67 \pm 0.61) \times 10^{-2}$	$(2.51 \pm 0.59) \times 10^{-2}$	$(2.47 \pm 0.58) \times 10^{-2}$	$(2.22 \pm 0.53) \times 10^{-2}$
2.25	$(1.86 \pm 0.43) \times 10^{-2}$	$(1.99 \pm 0.45) \times 10^{-2}$	$(2.02 \pm 0.46) \times 10^{-2}$	$(1.83 \pm 0.43) \times 10^{-2}$	$(1.51 \pm 0.37) \times 10^{-2}$
2.75	$(1.29 \pm 0.29) \times 10^{-2}$	$(1.39 \pm 0.32) \times 10^{-2}$	$(1.47 \pm 0.33) \times 10^{-2}$	$(1.37 \pm 0.31) \times 10^{-2}$	$(1.12 \pm 0.27) \times 10^{-2}$
3.25	$(9.62 \pm 0.22) \times 10^{-3}$	$(1.09 \pm 0.24) \times 10^{-2}$	$(1.08 \pm 0.24) \times 10^{-2}$	$(1.05 \pm 0.24) \times 10^{-2}$	$(8.48 \pm 2.03) \times 10^{-3}$
3.75	$(7.06 \pm 1.55) \times 10^{-3}$	$(8.05 \pm 1.80) \times 10^{-3}$	$(8.35 \pm 1.84) \times 10^{-3}$	$(8.52 \pm 1.88) \times 10^{-3}$	$(6.68 \pm 1.60) \times 10^{-3}$
4.50	$(4.70 \pm 1.02) \times 10^{-3}$	$(5.75 \pm 1.28) \times 10^{-3}$	$(6.02 \pm 1.33) \times 10^{-3}$	$(6.11 \pm 1.35) \times 10^{-3}$	$(5.10 \pm 1.20) \times 10^{-3}$
5.75	$(2.70 \pm 0.59) \times 10^{-3}$	$(3.56 \pm 0.79) \times 10^{-3}$	$(3.87 \pm 0.86) \times 10^{-3}$	$(3.99 \pm 0.88) \times 10^{-3}$	$(3.56 \pm 0.84) \times 10^{-3}$
7.25	$(1.45 \pm 0.32) \times 10^{-3}$	$(2.19 \pm 0.48) \times 10^{-3}$	$(2.36 \pm 0.52) \times 10^{-3}$	$(2.63 \pm 0.58) \times 10^{-3}$	$(2.36 \pm 0.56) \times 10^{-3}$
9.01	$(6.63 \pm 1.49) \times 10^{-4}$	$(1.01 \pm 0.23) \times 10^{-3}$	$(1.34 \pm 0.31) \times 10^{-3}$	$(1.32 \pm 0.30) \times 10^{-3}$	$(1.36 \pm 0.33) \times 10^{-3}$
11.2	$(2.68 \pm 0.64) \times 10^{-4}$	$(5.48 \pm 1.30) \times 10^{-4}$	$(6.78 \pm 1.65) \times 10^{-4}$	$(7.72 \pm 1.88) \times 10^{-4}$	$(7.65 \pm 1.98) \times 10^{-4}$
13.7	$(1.31 \pm 0.34) \times 10^{-4}$	$(3.29 \pm 0.85) \times 10^{-4}$	$(4.54 \pm 1.21) \times 10^{-4}$	$(5.61 \pm 1.49) \times 10^{-4}$	$(5.25 \pm 1.50) \times 10^{-4}$
16.2	$(6.73 \pm 1.79) \times 10^{-5}$	$(2.00 \pm 0.54) \times 10^{-4}$	$(3.10 \pm 0.86) \times 10^{-4}$	$(3.66 \pm 1.02) \times 10^{-4}$	$(2.83 \pm 0.95) \times 10^{-4}$
18.7	$(2.28 \pm 0.66) \times 10^{-5}$	$(9.85 \pm 2.95) \times 10^{-5}$	$(1.89 \pm 0.57) \times 10^{-4}$	$(2.12 \pm 0.66) \times 10^{-4}$	$(2.00 \pm 0.80) \times 10^{-4}$

resolution gets worse (see Figs. 10 and 11) as p_T increases.

The QCD-C background subtraction and the fitting procedure are sources of systematic uncertainty. The estimation of the fitting procedure uncertainty is similar to that for K_S^0 in MB events. The uncertainty from the QCD-C background subtraction is estimated by scaling the background by -25% from the default and recalculating the number of signal events. Similar to the K_S^0 in the MB events, the K_S^0 signal is clearly visible and the uncertainty is fairly constant at $\sim 12\%$ for all p_T and E_T intervals. For the Λ^0 baryon, the uncertainty increases by $\sim 2\%$ at the high p_T and E_T region, and we assign a conservative 17% for all p_T and E_T intervals. The total systematic uncertainty is the uncertainty discussed above and the uncertainty in the acceptance calculation added in quadrature.

The p_T distributions are calculated per jet, $1/N_{\text{jet}}dN/(p_T dp_T) = 1/N_{\text{jet}}\Delta N/(A p_T \Delta p_T)$, and are shown in Fig. 12 (K_S^0) and Fig. 13 ($\Lambda^0 + \bar{\Lambda}^0$) for the five jet- E_T intervals. N_{jet} is the number of jets in the E_T interval, ΔN is the number of signal events in the p_T interval (Δp_T) and E_T interval, and A is the acceptance at the p_T and E_T interval (Figs. 8 and 9). The uncertainty is the statistical and systematic uncertainties added in quadrature. The average jet- E_T values for the five jet- E_T intervals are 31, 50, 70, 99 and 136 GeV. Figure 14 shows $\Lambda^0 + \bar{\Lambda}^0$ to $2K_S^0$ ratios as a function of p_T calculated from Figs. 12 and 13. The K_S^0 cross section is multiplied by two to take into account the K_L^0 production. The ratios are about 0.25 for all p_T and E_T intervals.

The differential p_T distributions of K_S^0 and Λ^0 hadrons in jets are compared with the PYTHIA events generated with default parameters. The events from PYTHIA simulation, processed through CDF II detector simulation and

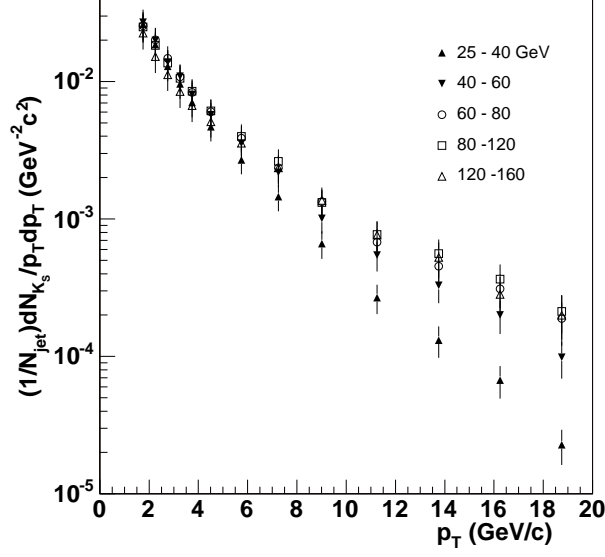


FIG. 12: The p_T distributions of K_S^0 mesons in centrally-produced jets ($|\eta| < 1$) for the five jet- E_T intervals. The uncertainties include both the statistical and systematic uncertainties added in quadrature.

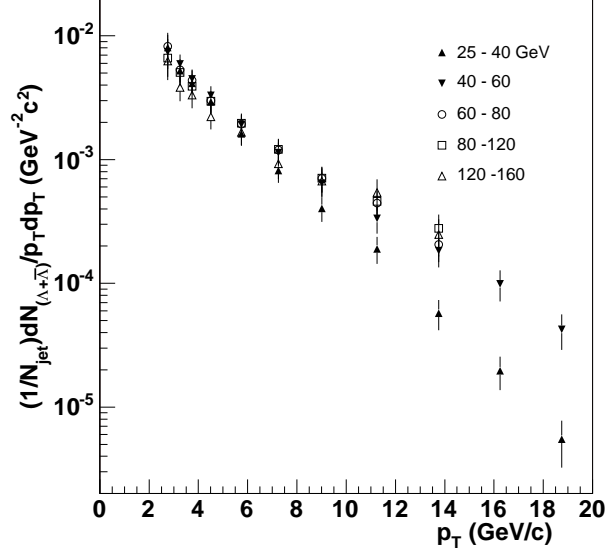


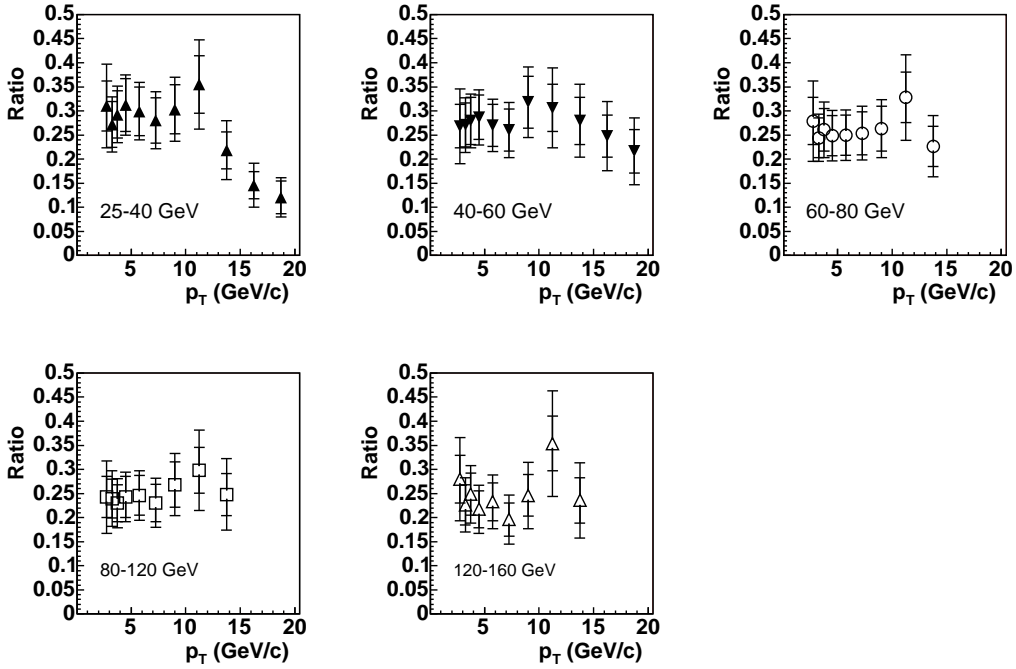
FIG. 13: The p_T distributions of $\Lambda^0 + \bar{\Lambda}^0$ baryons in centrally-produced jets ($|\eta| < 1$) for the five jet- E_T intervals. The uncertainties include both the statistical and systematic uncertainties added in quadrature.

reconstruction programs, are analyzed as the real data. However rather than finding the reconstructed number of resonances from fitting, the resonances at the particle generation level are used after associating them with reconstructed jets ($\Delta R < 0.5$) for the five jet- E_T intervals. Figure 15 shows the ratios of the K_S^0 of data to that of PYTHIA events as a function of p_T , and Fig. 16 shows the same for Λ^0 baryons. The agreement for Λ^0 baryons is adequate while PYTHIA generates too many K_S^0 mesons in the low p_T region.

Using the p_T distribution of Λ^0 baryons from an earlier analysis [15], and K_S^0 mesons from this analysis, the ratio of $\Lambda^0 + \bar{\Lambda}^0$ to $2K_S^0$ as a function of p_T in MB events is calculated and displayed in Fig. 17. In the same figure,

TABLE VI: The $\Lambda^0 + \bar{\Lambda}^0$ cross-section values for the five jet- E_T intervals in Fig. 13

$p_T(\text{GeV}/c)$	$1/N_{\text{jet}} dN/(p_T dp_T) (\text{GeV}^{-2} c^2)$				
	$E_T : 25\text{--}40 \text{ GeV}$	$40\text{--}60 \text{ GeV}$	$60\text{--}80 \text{ GeV}$	$80\text{--}120 \text{ GeV}$	$120\text{--}160 \text{ GeV}$
2.75	$(8.03 \pm 2.15) \times 10^{-3}$	$(7.42 \pm 2.02) \times 10^{-3}$	$(8.24 \pm 2.35) \times 10^{-3}$	$(6.62 \pm 1.96) \times 10^{-3}$	$(6.27 \pm 1.87) \times 10^{-3}$
3.25	$(5.23 \pm 1.00) \times 10^{-3}$	$(5.92 \pm 1.15) \times 10^{-3}$	$(5.30 \pm 1.16) \times 10^{-3}$	$(5.20 \pm 1.13) \times 10^{-3}$	$(3.84 \pm 0.89) \times 10^{-3}$
3.75	$(4.13 \pm 0.78) \times 10^{-3}$	$(4.50 \pm 0.85) \times 10^{-3}$	$(4.36 \pm 0.91) \times 10^{-3}$	$(3.92 \pm 0.82) \times 10^{-3}$	$(3.32 \pm 0.73) \times 10^{-3}$
4.50	$(2.93 \pm 0.55) \times 10^{-3}$	$(3.30 \pm 0.62) \times 10^{-3}$	$(3.00 \pm 0.60) \times 10^{-3}$	$(2.97 \pm 0.59) \times 10^{-3}$	$(2.22 \pm 0.47) \times 10^{-3}$
5.75	$(1.61 \pm 0.30) \times 10^{-3}$	$(1.92 \pm 0.36) \times 10^{-3}$	$(1.94 \pm 0.38) \times 10^{-3}$	$(1.96 \pm 0.39) \times 10^{-3}$	$(1.66 \pm 0.36) \times 10^{-3}$
7.25	$(8.16 \pm 1.67) \times 10^{-4}$	$(1.14 \pm 0.23) \times 10^{-3}$	$(1.20 \pm 0.26) \times 10^{-3}$	$(1.21 \pm 0.26) \times 10^{-3}$	$(9.24 \pm 2.29) \times 10^{-4}$
9.01	$(4.02 \pm 0.88) \times 10^{-4}$	$(6.44 \pm 1.41) \times 10^{-4}$	$(7.03 \pm 1.61) \times 10^{-4}$	$(7.08 \pm 1.68) \times 10^{-4}$	$(6.70 \pm 1.78) \times 10^{-4}$
11.2	$(1.90 \pm 0.48) \times 10^{-4}$	$(3.35 \pm 0.83) \times 10^{-4}$	$(4.45 \pm 1.11) \times 10^{-4}$	$(4.60 \pm 1.23) \times 10^{-4}$	$(5.41 \pm 1.53) \times 10^{-4}$
13.7	$(5.74 \pm 1.58) \times 10^{-5}$	$(1.84 \pm 0.49) \times 10^{-4}$	$(2.06 \pm 0.57) \times 10^{-4}$	$(2.78 \pm 0.82) \times 10^{-4}$	$(2.47 \pm 0.82) \times 10^{-4}$
16.2	$(1.97 \pm 0.60) \times 10^{-5}$	$(9.92 \pm 2.79) \times 10^{-5}$	-	-	-
18.7	$(5.50 \pm 2.27) \times 10^{-6}$	$(4.26 \pm 1.37) \times 10^{-5}$	-	-	-

FIG. 14: The cross-section ratios of $\Lambda^0 + \bar{\Lambda}^0$ to $2K_S^0$ as a function of p_T for the five jet- E_T intervals. There are two error bars for each data point. The inner (outer) one corresponds to the statistical (systematic) uncertainty.

the ratios from jets in Fig. 14 are also shown for a comparison. Also shown in the figure is the ratio from 1.8 TeV center-of-mass energy covering the very low p_T region [25]. The figure shows that the ratio of Λ^0 to K_S^0 exhibits different behavior than the $K^{*\pm}$ to K_S^0 and ϕ to K_S^0 ratios. For the latter, the ratios increase as p_T increases and reach a plateau at $p_T > 4 \sim 5 \text{ GeV}/c$, while the former increases until p_T reaches $\sim 2 \text{ GeV}/c$ and then decreases as p_T increases. The ratio plot also indicates that the process of producing Λ^0 baryons compared to K_S^0 mesons in MB events is significantly more efficient than the process in jets. The ratio from the MB events matches the ratios from jets at $p_T \sim 5 \text{ GeV}/c$ implying that QCD jet contribution is significant for $p_T > 5 \text{ GeV}/c$.

VII. SUMMARY

In inelastic $p\bar{p}$ collisions at $\sqrt{s} = 1.96 \text{ TeV}$, we have studied the properties of three mesons, K_S^0 , $K^{*\pm}$, and ϕ , in MB events up to $p_T = 10 \text{ GeV}/c$, and K_S^0 and Λ^0 hadrons in jets up to $20 \text{ GeV}/c$ p_T and 160 GeV jet E_T . The

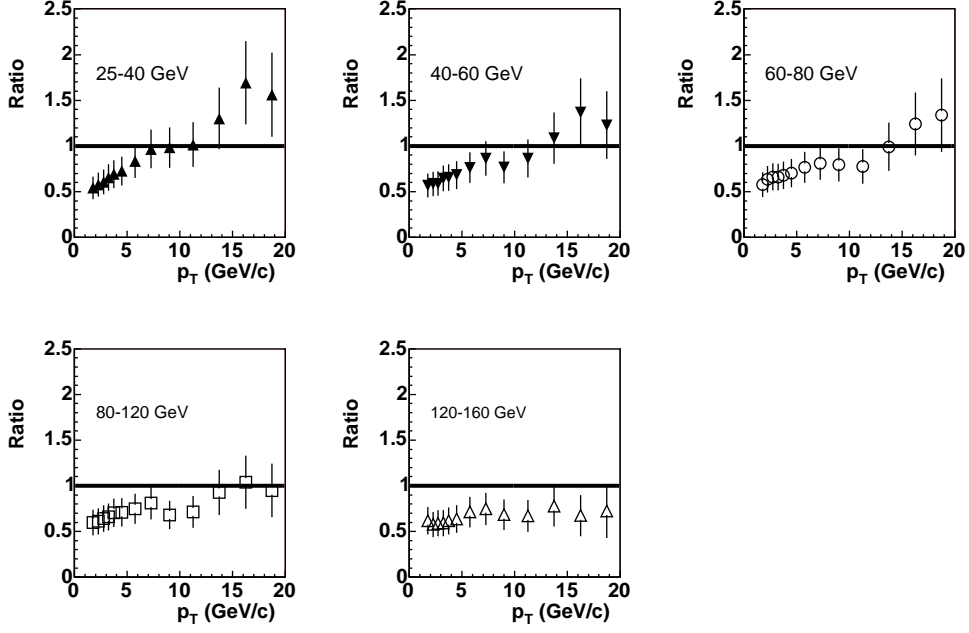


FIG. 15: The ratios of K_S^0 p_T distribution of data to that of PYTHIA (version 6) events generated with default parameters for the five jet- E_T intervals.

measurements were made with centrally produced ($|\eta| < 1$) particles and jets. We found in MB events:

1. As p_T increases, the three mesons exhibit a similar p_T slope as the n values indicate, where n is the exponent in the power law function.
2. The n values from the mesons are less than the values from hyperons (Λ^0 , Ξ^\pm , and Ω^\pm) by about 10%.
3. The ratios, $K^{*\pm}/2K_S^0$ and $\phi/2K_S^0$, as a function of p_T exhibit a similar behavior as $\Xi^\pm/(\Lambda^0 + \bar{\Lambda}^0)$ and $\Omega^\pm/(\Lambda^0 + \bar{\Lambda}^0)$ [15]. The ratios increase at low p_T and reach a plateau above $p_T \sim 5$ GeV/ c .
4. Unlike the ratios among strange mesons or hyperons, the Λ^0 to K_S^0 ratio shows an enhancement around 2 GeV/ c p_T .
5. PYTHIA reproduces ϕ p_T distribution quite well, but underestimates K_S^0 production and overestimates $K^{*\pm}$ production.

In jets:

6. The p_T dependencies of the K_S^0 and Λ^0 cross sections in jets reduce as jet E_T increases. The ratio, $(\Lambda^0 + \bar{\Lambda}^0)/2K_S^0$, is fairly constant at about 0.25 for p_T up to 20 GeV/ c and jet E_T up to 160 GeV. This ratio merges with the ratio from the MB events at $p_T > 4 \sim 5$ GeV/ c .
7. The process producing low p_T Λ^0 (compared to K_S^0) in MB events is significantly more efficient than the process in jets.
8. PYTHIA reproduces the Λ^0 p_T distribution reasonably well, but overestimates K_S^0 production in the low p_T region. The findings indicate that in MB events particles with p_T in excess of 5 GeV/ c are mostly from QCD jets, assuming that jets with $E_T < 25$ GeV behave similarly to the higher E_T jets. The process of producing Λ^0 compared to K_S^0 around 2 GeV/ c is much more efficient than the process in jets. Moreover while the production cross section exhibits strong dependences on the quark flavors (u , d , and s) in particles, the p_T slope for $p_T > 5$ GeV/ c is fairly insensitive to the number of quarks and quark flavors in particles, resulting in constant particle ratios. This suggests that p_T dependencies of particles produced in jets are similar regardless of their quark and flavor content.

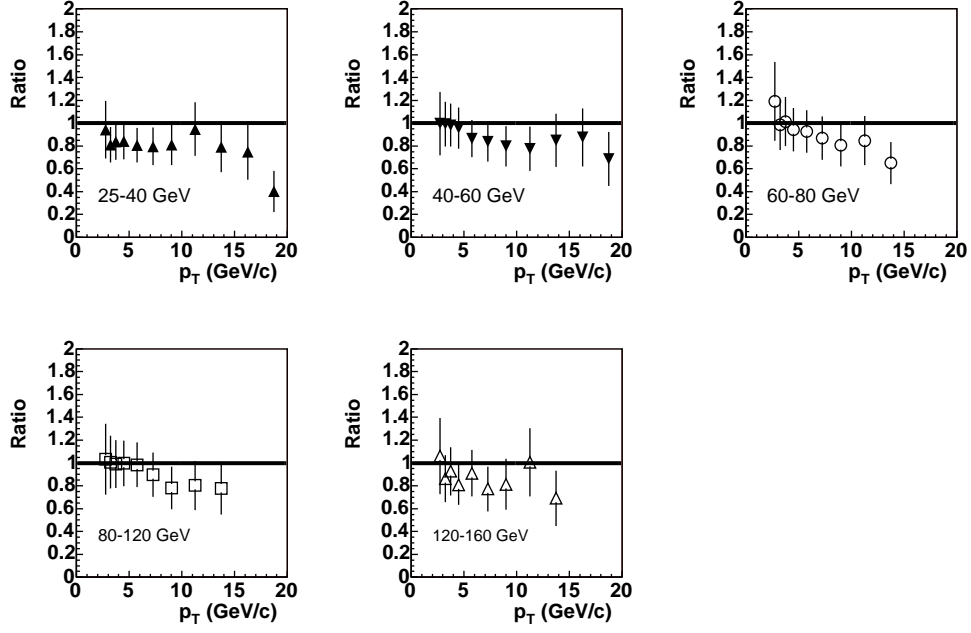


FIG. 16: The ratios of Λ^0 p_T distribution of data to that of PYTHIA (version 6) events generated with default parameters for the five jet- E_T intervals.

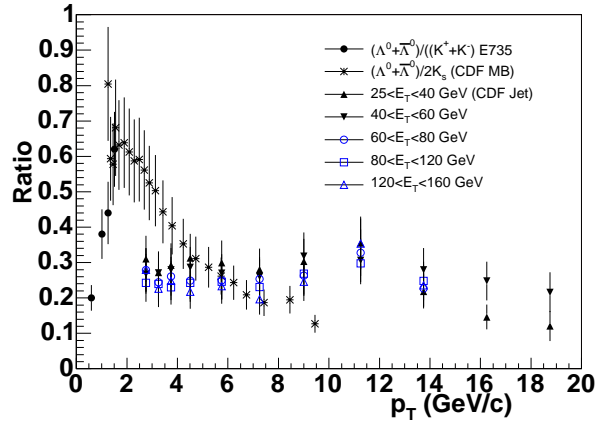


FIG. 17: The cross-section ratios of Λ^0 baryon to strange meson as a function of p_T . The data from E735 is also from the central region. The statistical and systematic uncertainties are added in quadrature.

We thank the Fermilab staff and the technical staffs of the participating institutions for their vital contributions. This work was supported by the U.S. Department of Energy and National Science Foundation; the Italian Istituto Nazionale di Fisica Nucleare; the Ministry of Education, Culture, Sports, Science and Technology of Japan; the Natural Sciences and Engineering Research Council of Canada; the National Science Council of the Republic of China; the Swiss National Science Foundation; the A.P. Sloan Foundation; the Bundesministerium für Bildung und Forschung, Germany; the Korean World Class University Program, the National Research Foundation of Korea; the Science and Technology Facilities Council and the Royal Society, UK; the Russian Foundation for Basic Research; the Ministerio de Ciencia e Innovación, and Programa Consolider-Ingenio 2010, Spain; the Slovak R&D Agency; the Academy of Finland; and the Australian Research Council (ARC).

-
- [1] T. Akesson *et al.* (AFS Collaboration) Phys. Lett. B **118**, 185 (1982).
- [2] M. Banner *et al.* (UA2 Collaboration) Phys. Lett. B **118**, 203 (1982); G. Arnison *et al.* (UA1 collaboration), Phys. Lett. B **123**, 115 (1983).
- [3] G.J. Alner *et al.* (UA5 Collaboration), Nucl. Phys. **B258**, 505 (1985); R.E. Ansorge *et al.* (UA5 Collaboration), Phys. Lett. B **199**, 311 (1987); T. Alexopoulos *et al.* (E735 Collaboration), Phys. Rev. Lett. **60**, 1622 (1988); F. Abe *et al.* (CDF Collaboration), Phys. Rev. Lett. **61**, 1819 (1988); R. Ansorge *et al.* (UA5 Collaboration), Nucl. Phys. **B328**, 36 (1989); G. Bocquet *et al.* (UA1 Collaboration), Phys. Lett. B **366**, 441 (1996); S. Banerjee *et al.* (E735 Collaboration), Phys. Rev. Lett. **64**, 991 (1990); D. Acosta *et al.* (CDF Collaboration), Phys. Rev. D **72**, 052001 (2005); B. I. Abelev *et al.* (STAR Collaboration), Phys. Rev. C **75**, 064901, (2007).
- [4] T. Sjöstrand, P. Eden, C. Friberg, L. Lonnblad, G. Miu, S. Mrenna, and E. Norrbin, Comput. Phys. Commun. **135**, 238 (2001). The version used in this paper is 6.327.
- [5] W. Braunschweig *et al.* (TASSO Collaboration), Z. Phys. C **47**, 167 (1990); H. Aihara *et al.* (TPC Collaboration), Phys. Rev. Lett. **54**, 274 (1985); H. Schellman *et al.* (MARK-II Collaboration), Phys. Rev. D **31**, 3013 (1985); M. Derrick *et al.* (HRS Collaboration), Phys. Rev. D **35**, 2639 (1987); H. Behrend *et al.* (CELLO Collaboration), Z. Phys. C **46**, 397 (1990); D. Buskulic *et al.* (ALEPH Collaboration), Z. Phys. C **64**, 361 (1994); P. Abreu *et al.* (DELPHI Collaboration), Z. Phys. C **65**, 587 (1995); M. Acciarri *et al.* (L3 Collaboration), Phys. Lett. B **328**, 223 (1994); P. Acton *et al.* (OPAL Collaboration), Phys. Lett. B **291**, 503 (1992).
- [6] M. Derrick *et al.* (ZEUS Collaboration), Z. Phys. C **68**, 29 (1995); S. Chekanov *et al.* (ZEUS Collaboration), Eur. Phys. J. C **51**, 1, (2001); S. Aid *et al.* (H1 Collaboration), Nucl. Phys. **B480**, 3 (1996); C. Adloff *et al.* (H1 Collaboration), Z. Phys. C **76**, 213 (1997).
- [7] A. Abulencia *et al.* (CDF Collaboration), J. Phys. G **34**, 2457 (2007).
- [8] A. Sill *et al.*, Nucl. Instrum. Methods A **447**, 1 (2000).
- [9] In the CDF coordinate system, θ and ϕ are the polar and azimuthal angles of a particle, respectively, defined with respect to the proton beam direction, z . The pseudorapidity η is defined as $-\ln[\tan(\theta/2)]$. The transverse-momentum of a particle is $p_T = p \sin \theta$. The rapidity is defined as $y = 0.5 \ln[(E + p_z)/(E - p_z)]$, where E and p_z are the energy and longitudinal momentum of the particle.
- [10] A. Affolder *et al.* (CDF Collaboration), Nucl. Instrum. Methods A **526**, 249 (2004).
- [11] L. Balka *et al.*, Nucl. Instrum. Methods A **267**, 272 (1988); S. Bertolucci *et al.*, Nucl. Instrum. Methods A **267**, 301 (1988); M. Albrow *et al.*, Nucl. Instrum. Methods A **480**, 524 (2002).
- [12] G. Apollinari *et al.*, Nucl. Instrum. Methods A **412**, 515 (1998).
- [13] D. Acosta *et al.*, Nucl. Instrum. Methods A **494**, 57 (2002).
- [14] A. Bhatti *et al.*, Nucl. Instrum. Methods A **566**, 375 (2006).
- [15] T. Aaltonen *et al.* (CDF Collaboration), Phys. Rev. D **86**, 012002 (2012). The n values are 8.81 ± 0.08 ($\Lambda^0 + \bar{\Lambda}^0$), 8.26 ± 0.12 (Ξ^\pm) and 8.06 ± 0.34 (Ω^\pm).
- [16] R. Brun, R. Hagelberg, M. Hansroul, and J. C. Lassalle, version 3.15, CERN-DD-78-2-REV.
- [17] C. Amsler *et al.* (Particle Data Group), Phys. Lett. B **667**, 1 (2008).
- [18] The total cross section corresponding to the MB trigger is estimated to be 45 ± 8 mb. The elastic (17 ± 4 mb [17]), single diffractive SD (12 mb), and half of the double diffractive DD (4 mb) cross sections are subtracted from the total $p\bar{p}$ cross section (78 ± 6 mb [17] [19]) to give this estimate. The SD and DD cross sections are estimated using PYTHIA [4], and no uncertainties are assigned to SD and DD cross section. A simulation study shows that the MB trigger is sensitive to $\sim 100\%$ of inelastic events which are not SD or DD and $\sim 50\%$ of DD events. A 100% uncertainty is assigned to the DD contribution due to the uncertainty in the event characteristics and detector simulation.
- [19] J.R. Cudell *et al.* (COMPETE Collaboration), Phys. Rev. Lett. **89**, 201801 (2002)
- [20] D. Acosta *et al.* (CDF Collaboration), Phys. Rev. D **71**, 032001 (2005).
- [21] F. Abe *et al.* (CDF Collaboration), Phys. Rev. Lett. **75**, 4358 (1995).
- [22] F. Abe *et al.* (CDF Collaboration), Phys. Rev. D **40**, 3791 (1989).
- [23] Private communication with one of PYTHIA authors.
- [24] T. Alexopoulos *et al.* (E735 Collaboration), Z. Phys. C **67**, 411416 (1995).
- [25] S. Banerjee *et al.* (E735 Collaboration), Phys. Rev. Lett. **62**, 12 (1989). T. Alexopoulos *et al.* (E735 Collaboration), Phys.

Rev. D 46, 2773 (1992).

This figure "logo_cdfii.gif" is available in "gif" format from:

<http://arxiv.org/ps/1308.3371v1>